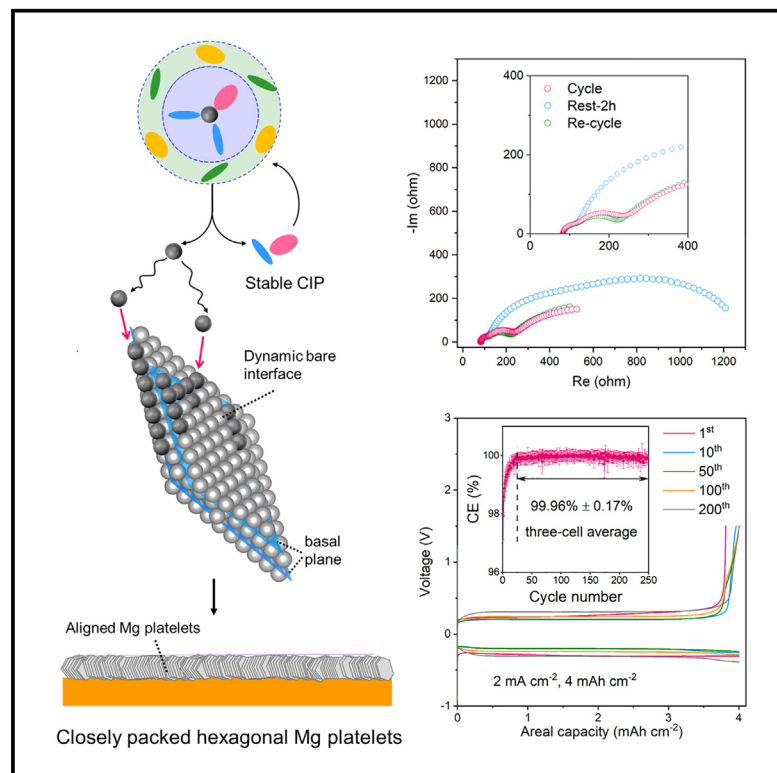


A dynamically bare metal interface enables reversible magnesium electrodeposition at 50 mAh cm^{-2}

Graphical abstract



Highlights

- An intrinsically stable electrolyte is designed for halide-free Mg batteries
- Near-unity CE of Mg plating/stripping achieved under very demanding conditions
- A unique, dynamically bare Mg/electrolyte interface exists during cycling
- Deposition of closely stacked hexagonal Mg platelets achieved at high rates

Authors

Chang Li, Rishabh D. Guha, Stephen D. House, ..., Kevin Zavadil, Kristin A. Persson, Linda F. Nazar

Correspondence

lfnazar@uwaterloo.ca

In brief

The presence of a solid electrolyte interphase in halogen-free magnesium electrolytes plagues the facile nucleation/growth of magnesium, causing its incomplete stripping with a Coulombic efficiency far below unity. Here, we report a phenomenon of dynamic, almost-bare magnesium/electrolyte interface formation that allows magnesium to spontaneously deposit into densely aligned, vertically stacked hexagonal platelets. This interface is kinetically stable due to the near-absent electrolyte decomposition during dynamic plating/stripping, leading to low interfacial resistance, rapid charge transfer, and near-unity Coulombic efficiency under demanding conditions.



Article

A dynamically bare metal interface enables reversible magnesium electrodeposition at 50 mAh cm⁻²

Chang Li,^{1,2} Rishabh D. Guha,³ Stephen D. House,^{2,4} J. David Bazak,^{2,5} Yue Yu,¹ Laidong Zhou,^{1,2} Kevin Zavadil,^{2,6} Kristin A. Persson,^{3,7} and Linda F. Nazar^{1,2,8,*}

¹Department of Chemistry and the Waterloo Institute for Nanotechnology, University of Waterloo, Waterloo, ON N2L 3G1, Canada

²Joint Center for Energy Storage Research, Argonne National Laboratory, Lemont, IL 60439, USA

³Materials Science Division, Lawrence Berkeley National Laboratory, Berkeley, CA 94720, USA

⁴Center for Integrated Nanotechnologies, Sandia National Laboratories, Albuquerque, NM 87123, USA

⁵Physical & Computational Science Directorate, Pacific Northwest National Laboratory, Richland, WA 99354, USA

⁶Material, Physical and Chemical Sciences Center, Sandia National Laboratories, Albuquerque, NM 87185, USA

⁷Department of Materials Science and Engineering, UC Berkeley, Berkeley, CA 94720, USA

⁸Lead contact

*Correspondence: lfnazar@uwaterloo.ca

<https://doi.org/10.1016/j.joule.2024.11.007>

CONTEXT & SCALE Mg anodes suffer from insufficient electrodeposition/stripping (E/S) efficiency in common halogen-free electrolytes at high areal capacities and high rates. The formation of a Mg²⁺-insulating solid electrolyte interphase (SEI) due to electrolyte decomposition is a major stumbling block under demanding conditions. Here, we report a new, intrinsically stable electrolyte that tackles this challenge by generating a dynamically free SEI—revealed by advanced microscopy and spectroscopy—during the net E/S. The effectively bare Mg/electrolyte interface leads to fast Mg nucleation/growth into thin platelets at high deposition rates, showing near-unity E/S efficiency at capacities of up to 50 mAh cm⁻². Our fundamental understanding of the ternary relationship of electrolyte-interphase-morphology is distinct from conventional SEI concepts. It opens a new avenue to the efficient utilization of multivalent cations that are often plagued with poor reversibility/kinetics in electrochemical cells.

SUMMARY

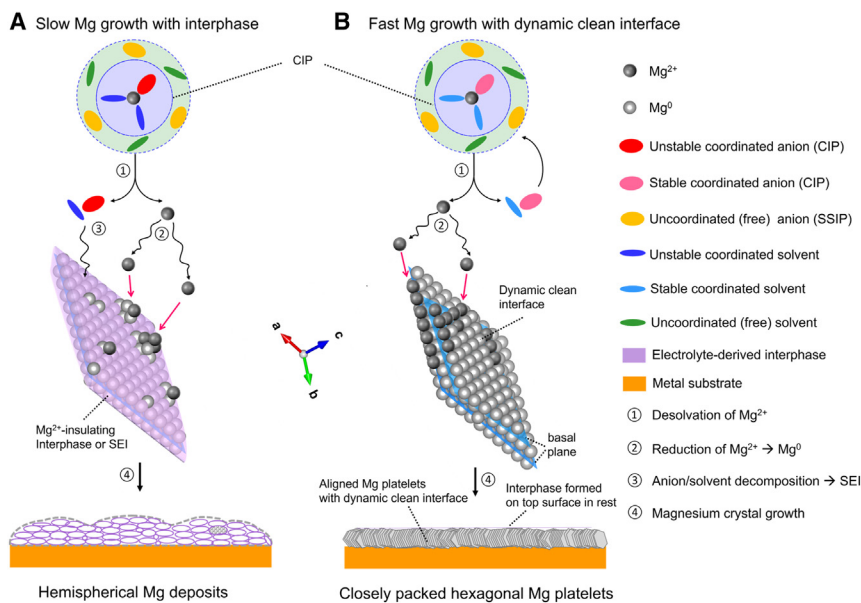
Understanding and facilitating pure magnesium nucleation/growth electrodeposition behavior with ultrahigh Coulombic efficiency is complicated by the phenomenon of solid electrolyte interphase (SEI) formation in state-of-the-art, halogen-free magnesium electrolytes. Defining the electrolyte properties necessary to achieve ideal electrodeposition/stripping (E/S) thus remains elusive. Here, we reveal for the first time, rapid magnesium electrodeposition behavior that forms densely aligned, micron-sized thin platelets by establishing a dynamic bare magnesium/electrolyte interface during high-rate net plating. This effectively “SEI-free” interface allows facile magnesium diffusion and migration in stripping with near-unity E/S efficiency under demanding conditions over long-term cycling. The intrinsic electrolyte stability of the salt/solvent at the molecular level is the key to forming such an interface. The efficacy of the dynamic bare interface and an electrodeposited, free-standing magnesium anode is demonstrated in a high-areal-capacity full cell. These findings provide new design principles and fundamental understanding of interfacial chemistry in multivalent metal batteries.

INTRODUCTION

Rechargeable magnesium batteries (RMBs) are considered to be potential alternatives to lithium-ion batteries due to the wide crustal abundance of magnesium, its suitable potential, safety, and its high volumetric capacity (3,833 mAh cm⁻³).^{1–6} Magnesium elec-

trodeposition/stripping (E/S) can be achieved in conventional chloride-based magnesium electrolytes that obviate passivation layer formation,^{7,8} but they suffer from low oxidative stability and high corrosivity to battery components. Considerable effort has been devoted to trying to achieve efficient magnesium metal E/S in halide-free electrolytes. The challenges encountered with the





Scheme 1. Schematic illustration of interphase/interface guided magnesium growth pattern at high deposition rates

(A) Typical slow 3D growth into hemispherical morphology induced by Mg^{2+} -insulating interphases or solid electrolyte interphases (SEIs) in the state-of-art halide-free electrolytes, including carborane/alkoxyborate/ $Mg(TFSI)_2/Mg(OTf)_2$ -based electrolytes.

(B) Fast $(0001)_{Mg}$ growth into hexagonal platelets enabled by a dynamic clean interface with thermodynamically/kinetically stable solvation sheath.

reactivity.^{7,11,12,17,31,32,40–44} Nonetheless, depending on the thickness, composition, and uniformity, these interphases are either Mg^{2+} -insulating passivation layers or exhibit slow solid-state Mg^{2+} diffusion as SEIs.^{39,45} Either case can hinder natural magnesium growth on the $(0001)_{Mg}$ basal plane (Scheme 1A). Instead, free magnesium ions tend to adsorb on the

decomposition of most conventional electrolytes due to contact-ion pairs (CIPs)⁹—which passivate the anode surface and induce low Coulombic efficiency (CE) of magnesium E/S—mean that these endeavors have been largely unsuccessful to date at high areal capacities and current densities.^{1,10–17} Unconventional bulky carborane and boron/aluminum-alkoxy anions were thus designed to weakly coordinate Mg^{2+} , showing greatly enhanced electrolyte stability up to 4 V and highly efficient E/S with over 99% CE.^{18–25} These can be promising strategies once lowering the cost of synthesis and the issue of commercial availability is addressed.²⁶ Magnesium also historically has a lower tendency to form dendrites, which are the Achilles' heel for many metal anodes such as lithium, sodium, and zinc.²⁷ Some rationales for this behavior are based on findings from density functional theory (DFT) calculations that report (1) a very low surface energy of the $(0001)_{Mg}$ basal plane in the hexagonal $P6_3/mmc$ space group^{28,29} and (2) strong Mg^0 - Mg^0 bonding that favors high dimensional phases.³⁰ The second point is proven by three-dimensional (3D) hemispherical growth of Mg deposits in state-of-the-art halide-free electrolytes, including carborane/organoborate- and bis(trifluoromethanesulfonimide)(TFSI)-based electrolytes.^{9,31,32} However, evidence for the first point—the very low surface energy of the $(0001)_{Mg}$ plane—has not been experimentally observed in these halide-free systems even with good E/S efficiency.^{11–17,33} Taking advantage of this could be key to realize high-functioning divalent metal anodes (both Mg and Zn) at practical conditions.^{34–37}

In lithium batteries, the presence of a solid electrolyte interphase (SEI) allows Li^+ ions to migrate through it but prevents lithium from (electro)chemically reacting with the electrolyte by blocking electron transfer.³⁸ Unlike Li^+ , the divalent nature of Mg^{2+} makes it difficult to tunnel through such interphases at ambient conditions, which thus increase interfacial impedance in most cases.³⁹ Various functional artificial/*in situ* interphases have been reported to protect magnesium from such detrimental

exposed fresh magnesium nucleation sites due to the strong Mg^0 - Mg^0 bond,³⁰ favoring 3D growth to typically form hemispherical morphologies that could cause short circuits.¹⁰ The presence of Mg^{2+} -insulating interphases can also lead to uneven stripping behavior, as previously reported.^{46,47} Therefore, achieving reversible E/S at significant volumes of magnesium that can be sustained on long-term cycling with >99.9% cycling efficiency is still a major stumbling block on the path to practical halide-free rechargeable batteries.^{48,49}

Here, we demonstrate that forming a dynamic clean interface unlocks rapid magnesium nucleation/growth along the edges of $(0001)_{Mg}$, which has the lowest surface energy and self-diffusion barrier (Scheme 1B).^{28,29,50} This results in the deposition of closely stacked, aligned, and thin hexagonal platelets on the substrate at high plating rates. The formation of such a clean interface originates from the thermodynamically/kinetically stable CIPs within a carefully tuned solvent mixture that leads to nearly free electrolyte decomposition during dynamic magnesium plating. Such a clean interface shows the very low interfacial resistance that exists during dynamic electrochemical cycling—which disappears on rest and is restored by pulsing the current. In the absence of a thick interphase, the magnesium deposition is fully strippable with near-unity CE (up to 99.96%) at practical current densities ($2\text{--}5\text{ mA cm}^{-2}$) and areal capacities ($4\text{--}50\text{ mAh cm}^{-2}$) and shows stable cycling in 2 mAh cm^{-2} full cells with high-voltage cathodes.

RESULTS AND DISCUSSION

A dynamic bare interface guides dense magnesium electrodeposition

We first review the magnesium deposition morphologies in typical organoborate salt and $Mg(TFSI)_2$ -based electrolytes that show $\sim 4\text{ V}$ anodic stability.^{9,31} Although very different magnesium E/S CE of $\sim 98\%$ and $\sim 70\%$ was obtained for these electrolytes,

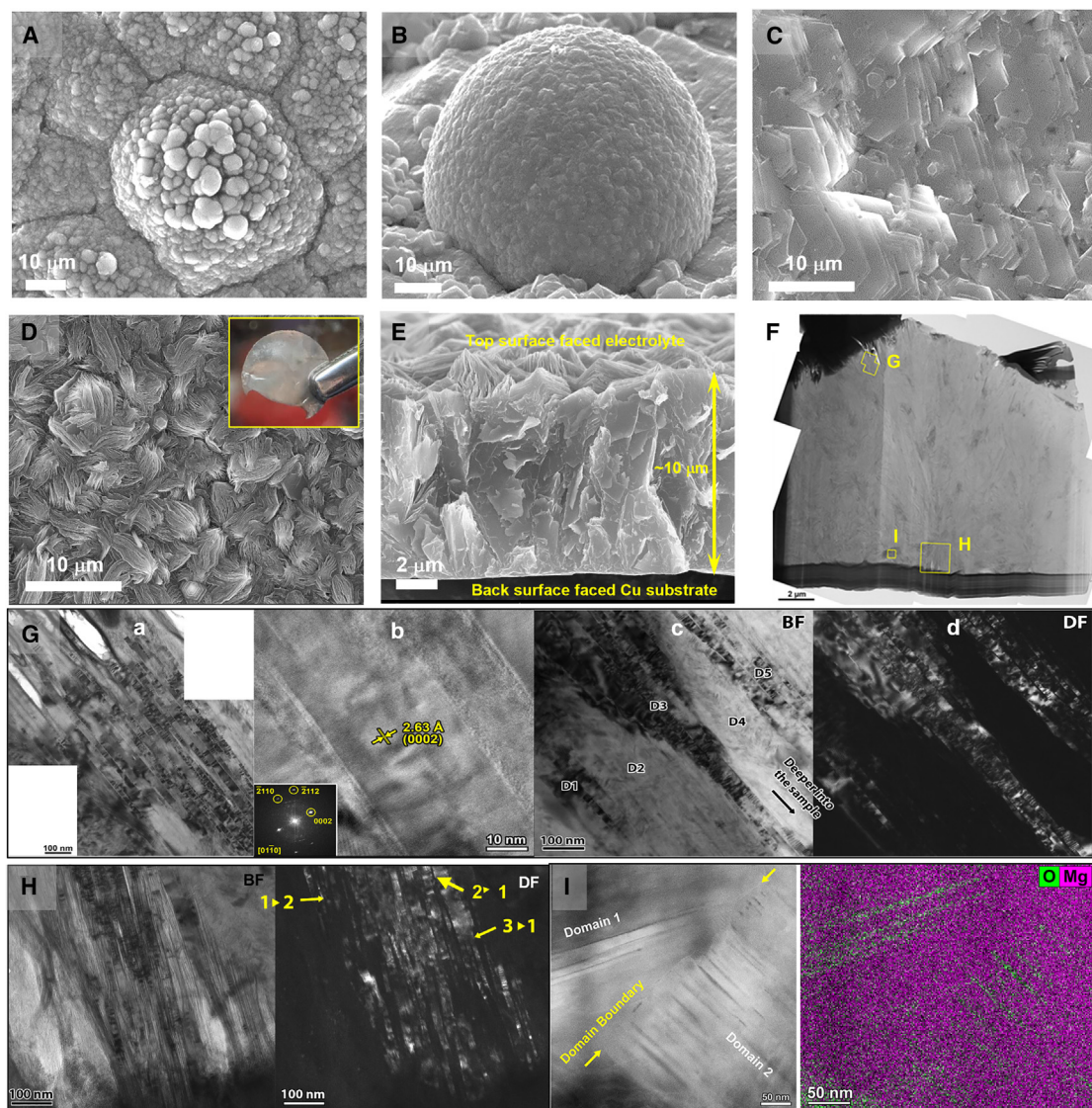


Figure 1. Role of interfacial chemistry in magnesium deposition morphology

(A–C) SEM images of magnesium deposition in (A) 0.2 M magnesium hexafluoroisopropoxy borate ($\text{Mg}(\text{B}(\text{hfp})_4)_2/\text{G}2$), (B) 0.5 M $\text{Mg}(\text{TFSI})_2/\text{DME}:\text{TEP}$, and (C) 0.2 M $\text{Mg}(\text{OTf})_2/\text{G}2:\text{TEP}$ at 0.5 mA cm^{-2} (0.5 mAh cm^{-2}).

(D and E) SEM images of magnesium deposition in 0.2 M $\text{Mg}(\text{OTf})_2/\text{G}2:\text{TEP}$ at 2 mA cm^{-2} and 4 mA cm^{-2} . The inset image corresponds to this thin Mg foil that easily detaches from the Cu substrate as shown in Video S1.

(F) TEM images of a FIB-cut sample in (E).

(G) BF-TEM images of (a) the surface fissure-to-lath transition region and (b) lattice-resolution close-up of a lath and corresponding FFT diffractogram (inset); (c and d) BF/DF-TEM micrograph pair of multiple adjacent lath domains (D1–5) near fissure, showing the nucleation and growth (e.g., D3) or shrinkage (e.g., D2 and D4) of lath domains.

(H) BF/DF-TEM micrograph-paired images of the nucleation region close to Cu substrate, showing widening ($1 \rightarrow 2$), narrowing ($3 \rightarrow 1$), and termination of the laths during the growth process as indicated by yellow arrows.

(I) HAADF-STEM image of two lath domains and corresponding STEM-EDS spectral image, showing extremely low levels of F, S, and P (<0.1 atom %) as shown in Figure S14) at the respective internal interfaces and suggesting negligible electrolyte decomposition during the dynamic E/S period.

respectively, classic 3D hemispherical growth was observed in both electrolytes (Figures 1A and 1B) due to interphase formation at the magnesium surface. Such electrolyte-derived interphases have been widely reported and examined in a range of halide-free electrolytes.^{11–16,26,51} Simply by adroitly tuning the molecular

structure of salt and solvent in the electrolyte, we successfully obviate such interphase formation and achieve magnesium (0001) growth in a 0.2 M magnesium trifluoromethanesulfonate ($\text{Mg}(\text{OTf})_2$)/diglyme (G2) : triethyl phosphate (TEP). This system was rationally designed for each electrolyte component at the

molecular level so that the stability against reduction of coordinated solvents and anions in CIPs can be maximized, as illustrated in Figure S1 and Note S1. Simple screening experiments were also conducted to determine the best ratio of each electrolyte component (Figure S2). Our results show that such precise control results in remarkable morphological and electrochemical properties compared with previous studies of halide-free systems (see below). We observed that hexagonal magnesium crystals deposit parallel to the substrate at a moderate current density of 0.5 mA cm^{-2} (Figures 1C and S3), similar to observations in some chloride-related systems.^{34,50} The magnesium morphology at a high current density of 2 mA cm^{-2} and an areal capacity of 4 mAh cm^{-2} is quite different, however, and more important from a practical perspective. Cross-sectional scanning electron microscopy (SEM) images reveal thin, micron-sized magnesium platelets aligned at an angle with respect to the substrate (Figures 1D, 1E, and S4), which stack to form a densely packed layer with near-theoretical density. A $10\text{-}\mu\text{m}$ -thick magnesium metal foil was obtained upon plating, which readily detached from the Cu substrate when immersed in dimethoxyethane (DME) (Figures 1D, 1E, S5, and S6; Video S1). The characteristics of very dense deposition and loose attachment with the substrate resulting from this unique growth pattern can potentially be used for electrodepositing free-standing magnesium metal foils (see below) to fulfill high-energy-density requirements for RMBs.^{52,53} Producing such foils via mechanical processing is challenging because pure magnesium is brittle and fragile. The Mg (0001) growth pattern sharply contrasts with the texture-free, 3D hemispherical morphologies exhibited in halide-free electrolytes (Figures 1A and 1B),^{11,12,17,29,30} where an artificial or *in situ* functional SEI is reported to form on the deposited magnesium surface.

We confirmed the dense Mg morphology by examining the bulk structure and composition of the electrodeposited magnesium using analytical transmission electron microscopy (TEM) to characterize cross-sections of the deposit at 2 mA cm^{-2} and 4 mAh cm^{-2} . Details of sample preparation and analysis are provided in the experimental procedures and Figure S7. We find that the magnesium crystallites are ensembles of finer-scale crystalline domains characterized by a parallel lath structure (Figures 1F and S8). This microstructure dominates through the entirety of the $10\text{-}\mu\text{m}$ -thick deposit. We note that the outermost region of the ensembles ($\leq 1 \mu\text{m}$ below the deposit surface) contains fissures that run parallel to the finer-scale laths (Figures 1Ga and S9) and are likely a consequence of competitive growth dynamics of the underlying laths themselves. Most of these lath-lath boundaries appear continuous, only occasionally exhibiting an elongated void or inclusion running parallel to the laths (Figure S10). These laths grow consistently in the [1000] direction to form $\sim 30 \text{ nm}$ -thin hexagonal platelets stacked parallel to the (0001)_{Mg} basal plane, propagating at pyramidal planes as confirmed through diffraction analysis (Figures 1Gb and S8). Consistent with this structural model is the presence of long propagation distances of lath domains (Figure S9), with lath widening, narrowing, termination, and re-nucleation occurring throughout the whole bulk deposit in both the initial nucleation (Figure 1H) and subsequent growth regions (Figures 1Gc and 1Gd). This indicates the existence of dynamic clean interface chemistry during the net plating process,

where no significant interphase forms to hinder the facile nucleation/growth behavior. Clearly, ion depletion—which would induce dendrite growth—does not occur even at high plating rates. The innermost region of the nodule ($>9 \mu\text{m}$ below the deposit surface) contains smaller-scale laths in smaller-sized domains, along with a low density of voids emanating from the original Mg deposit/Cu substrate interface (Figures 1H and S11). These features are consistent with this region being one of nucleation and early-stage competitive growth. Overall, plating at 2 mA cm^{-2} produces a dense, crystalline magnesium deposit.

Parasitic decomposition of the electrolyte and impurity incorporation in the deposit is quite limited. Scanning transmission electron microscopy-energy-dispersive X-ray spectroscopy (STEM-EDS) imaging of the (1) fissure/void transition region (Figure S12), (2) interfacial voids in the nucleation region (Figure S13), and (3) lath domain boundaries throughout the bulk (Figures 2I and S14) yield signatures for extremely low levels of F, S, and P ($<0.1 \text{ atom } \%$) at the respective internal interfaces, which are chemical markers for the OTf[−] anion and the TEP coordinating solvent. The presence of trace oxides is possibly from the trace impurity/moisture in the electrolyte^{54,55} or minor air exposure (see experimental procedures). As these buried interface-forming inclusions are produced during deposition, this finding indicates that the electrolyte supports near-free-interphase magnesium deposition, exhibiting a *dynamic* clean interface during the cycling. At the very top surface of the fissure region—where lath growth ends—depth-profiling X-ray photoelectron spectroscopy (XPS; Mg 1s, S 2p, F 1s, P 2p, and C 1s) reveals an ultrathin interphase that likely forms due to equilibration between the electrolyte and freshly deposited superficial magnesium during the rest period (Figure S15). However, it does not affect the behavior of the dynamic clean interface during the net E/S and its efficiency (see below). The lack of structure related to impurities and resulting passivation can enable exhaustive stripping of magnesium, preventing localized deposition and ensuring formation of a dense, crystalline deposit after repeated cycling. The reversibility and stability of magnesium E/S is thus maximized by such a magnesium (0001) deposition pattern.

To confirm the absence of any electrolyte-derived interphase in the bulk of the magnesium deposit in the Mg(OTf)₂/G2:TEP electrolyte, we further performed depth-profiling time-of-flight secondary ion mass spectrometry (TOF-SIMS) studies (Figure 2A). A similar analysis was also conducted on plated magnesium in the Mg(TFSI)₂/DME:TEP electrolyte for direct comparison. All data points collected in 3D space were summed into 2D XZ and YZ planes to alleviate the variance of homogeneity of different morphologies of plated magnesium. In the Mg(OTf)₂/G2:TEP electrolyte (Figures 2B and S16), F[−] species can be found on the surface of the magnesium deposited, with an areal capacity of 4 mAh cm^{-2} at a current density of 2 mA cm^{-2} , but are absent in the bulk region. The S[−] species shows the same behavior but with less intensity compared with the F[−]. These results are consistent with the previous TEM-EDS (Figure 1I) and XPS (Figure S15) results, showing the absence of an electrolyte-derived interphase in the bulk region that suggests the presence of an “effectively bare” magnesium/electrolyte interface during plating. These results, together with the XPS above, support our conclusion that the interphase only forms at the surface, where the fissures form. In

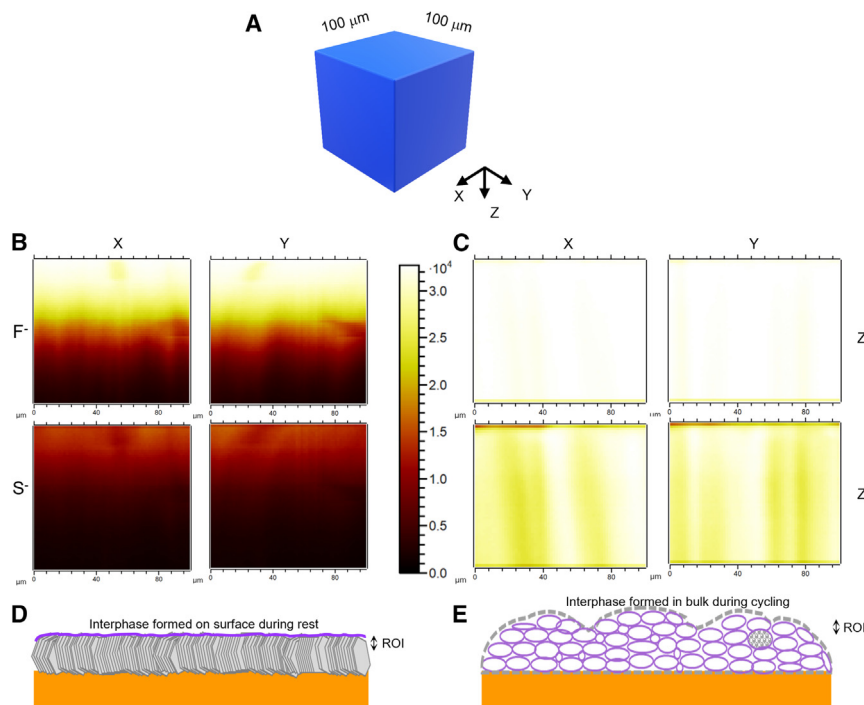


Figure 2. TOF-SIMS studies of interphase chemistry on deposited Mg surface

(A) Scheme of 3D TOF-SIMS analysis. A $100 \times 100 \mu\text{m}^2$ area on the top surface (XY plane) was selected as the region of interest, where the ion sputtering was performed in the Z direction. (B and C) The summed distribution of F^- and S^- in XZ and YZ plane in (B) 0.2 M $\text{Mg}(\text{OTf})_2/\text{G2}:\text{TEP}$ and (C) 0.5 M $\text{Mg}(\text{TFSI})_2/\text{DME}:\text{TEP}$. (D and E) Schematic illustrations of interphase-controlled magnesium deposition morphologies with estimated region of interest (ROI) in (D) 0.2 M $\text{Mg}(\text{OTf})_2/\text{G2}:\text{TEP}$ and (E) 0.5 M $\text{Mg}(\text{TFSI})_2/\text{DME}:\text{TEP}$.

contrast, in the $\text{Mg}(\text{TFSI})_2/\text{DME}:\text{TEP}$ electrolyte (Figures 2C and S16), both F^- and S^- species are distributed with much higher intensity on both the top surface and in the bulk of the magnesium deposit, suggesting that interphases were formed during magnesium plating. The variance of interphase formation/distribution leads to the very different morphology vis a vis the $\text{Mg}(\text{OTf})_2/\text{G2}:\text{TEP}$ electrolyte. In the latter, interphases formed only on the surface can be ascribed to the equilibration process during the rest and do not interrupt the spontaneous magnesium growth into closely packed hexagonal platelets during the dynamic plating period (Figure 2D). However, in $\text{Mg}(\text{TFSI})_2/\text{DME}:\text{TEP}$, the significant interphase formation in the bulk (Figure 2E) during magnesium plating greatly hinders such growth behavior due to the very slow migration of Mg^{2+} through the interphase, thus resulting in a hemispherical morphology.

Near-unity CE of magnesium electrodeposition/stripping

To investigate the magnesium E/S behavior, $\text{Mg}|\text{Cu}$ cells were subjected to galvanostatic cycling at a realistic current density of 2 mA cm^{-2} . Figure 3A shows that an ultrahigh plating capacity of over 50 mAh cm^{-2} (based on Cu electrode area) can be achieved at a low overpotential of $\sim 250 \text{ mV}$. This corresponds to a magnesium utilization rate (MUR) of up to 94.3%, and the plated magnesium can be reversibly stripped with a high CE of 98.6%. The long-term magnesium E/S was further examined at various conditions (Figures 3B and S17). At a fixed areal capacity of 4 mAh cm^{-2} to adhere to practical cycling protocols (Figures 3B and 3C), a high initial CE of $\sim 98\%$ was achieved at 2 mA cm^{-2} , which quickly increased to over 99.9% after 20 cycles and was maintained for over 250 cycles. This results in an unprecedented average CE of

$99.96\% \pm 0.17\%$ (after 20 cycles). The very stable E/S profiles throughout the entire measurement rule out the possibility of any soft shorts (Figures 3B and 3C).⁵⁶ The gentle curve at the end of stripping is similar to that seen in many previous studies. It is due to alloying between Mg and the Cu substrate,^{30,42,54} in contrast to the Au substrate, which does not alloy (Figure S18). An average 99.8% CE can still be achieved at an areal capacity or current density of up to 10 mAh cm^{-2} or 5 mA cm^{-2}

(Figures S17 and S19), respectively. Similar near-unity CE was also obtained by adopting a modified Aurbach method (Figure S20). The excellent stability of magnesium E/S is also confirmed in a $\text{Mg}|\text{Mg}$ cell at 4 mAh cm^{-2} that operates for over 2,000 h at 1 mA cm^{-2} (Figure 3D). The overpotential at 2 mA cm^{-2} is only slightly higher than that at half the current density, indicating very good kinetics. At a high current density of 5 mA cm^{-2} , the cell still functions for up to 700 h. The stable cycling of symmetric cells is also demonstrated at an ultrahigh areal capacity of 20 mAh cm^{-2} for over 450 h (Figure S21). To the best of our knowledge, this is the first demonstration of such promising performance under practical electrochemical protocols (Figure 3E). We attribute these outstanding E/S behaviors to the dynamic clean interface that induces fast magnesium (0001) growth and the subsequent unconstrained stripping process, as Mg^{2+} solid-state diffusion is not blocked or thwarted by a thick interphase.

We verified the presence of dynamic bare metal interface by impedance analysis. We observed that the interfacial resistance increased during the rest period (Figures 3F and S22), indicating a new interphase formed on the freshly deposited magnesium surface close to the fissure region; however, it reverted back to its original state after reversing the E/S current. These results confirm that a dynamic interfacial chemistry exists during the net E/S with fast charge transfer kinetics, consistent with the TEM analysis (Figures 1F–1I). Such behavior is not affected by the interphase formed at rest, as further verified by the stable and similar $\sim 100\%$ CE of magnesium E/S with the addition of open-circuit voltage (OCV) period after each plating (Figure 3G).^{24,57} It is worthy to note that the stability and reversibility of magnesium E/S is greatly compromised upon simply changing the salt from $\text{Mg}(\text{OTf})_2$ to the more common $\text{Mg}(\text{TFSI})_2$,

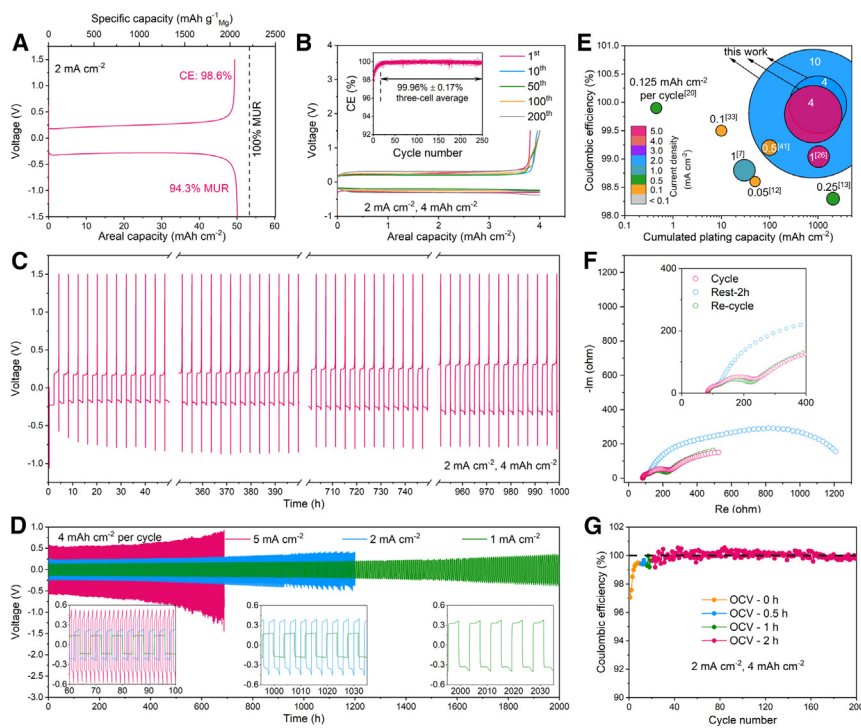


Figure 3. The electrochemical performance of magnesium electrodeposition/stripping

(A) Voltage profiles of a Mg||Cu cell at 2 mA cm^{-2} with cutoff voltages of -1.5 and 1.5 V at plating and stripping, respectively, showing the magnesium utilization rate (MUR) of 94.3%.

(B) Selected voltage profiles of a Mg||Cu cell at 2 mA cm^{-2} with a fixed areal capacity of 4 mAh cm^{-2} . The inset shows the corresponding evolution of CE as a function of cycle number, where solid circles and error bars are the mean and standard deviation of three independent cells, respectively.

(C) Stable and continuous voltage profiles of Mg||Cu cell at 2 mA cm^{-2} (4 mAh cm^{-2}) show no sign of soft shorts.

(D) Long-term stability of magnesium E/S in Mg||Mg cells at various current densities with an areal capacity of 4 mAh cm^{-2} .

(E) Comparison of the electrochemical performance with that reported in the literature (Table S1). The size and color of each circle correspond to as-labeled areal capacity per cycle and current density, respectively.

(F) The EIS spectra of a Mg||Mg cell measured after cycling, resting for 2 h, and re-cycling period. Full measurement and analysis can be seen in Figure S22.

(G) The CE evolution as a function of cycle numbers with different OCV periods after each plating.

suggesting the significantly higher electrochemical stability of the triflate anion that spurred our investigation below. Direct electrochemical comparison of the two salts and additional SEM images of Mg deposit morphology are given in Figures S23A–S23D.

High electrochemical stability of the electrolyte

We attribute the dynamic clean interface to the high electrochemical stability of the electrolyte, which directly relates to its solvation structure and nature of the CIPs. The electrolyte solvation dynamics were investigated by nuclear magnetic resonance (NMR) spectroscopy, combined with DFT calculations and molecular dynamic (MD) simulations to unravel the molecular behavior underpinning the intrinsic stability of the electrolyte. ^{31}P variable-temperature (VT) NMR was performed to examine the role of the TEP in coordinating the Mg^{2+} cations and the interaction of the solvation shell with the counter anions participating in CIP formation. The commonly studied Mg(TFSI) $_2$ system was used as a comparison. Figures 4A and 4B show stack plots for both the TFSI and OTf compositions that span the temperature regime from 313 to 243 K. As the temperature is decreased, the lone ^{31}P signal splits to reveal a distinct, low-T signal at lower frequency. In contrast, in neat G2/TEP at the same ratio (Figure S24), the ^{31}P VT-NMR peaks appear at higher frequency and with a characteristic ^1H - ^{31}P scalar coupling septet. The lack of scalar coupling in Figures 4A and 4B is due to reduced tumbling imparted by the coordination to the salt and the inductive effect of anion participation in the solvation shell. This identifies the secondary, low-T ^{31}P signal as the CIP formed with TEP-coordinated Mg^{2+} . As the temperature is decreased, the anion exchange rate in the equilibrium solvation structure correspondingly moves to a “slow exchange” regime.⁵⁸

A key difference is immediately apparent between the TFSI and OTf compositions, reflected quantitatively in the VT ^{31}P T_2 measurements of the corresponding signals (Figures 4C and 4D). Whereas the TFSI composition undergoes a classical exchange transition—first exhibiting broadening, then coalescence, and finally splitting of signals as the exchange rate slows with decreasing temperature—the OTf composition inversely shows very little exchange broadening before bifurcation and a significantly smaller relative CIP population once the signal splits. This indicates that the lifetime of the OTf CIPs is much shorter. The CIP interaction is therefore much weaker, correlating with the much-reduced electrolyte decomposition and “clean” reversible Mg deposition. The T_2 magnitudes for both electrolytes are considerably shorter than TEP in the neat G2/TEP mixture (Figure S25), indicative of TEP coordination to the cation itself in both cases, as proven by DFT studies (see below). Additional ^{31}P exchange spectroscopy (EXSY), ^{19}F T_2 relaxation, and ^{19}F pulsed-field gradient (PFG-NMR) diffusivity measurements also bear out this difference between the electrolyte compositions (see Figures S26–S30 and accompanying discussion in Note S2).

Results from classical MD (Figure S31) vindicate the experimental evidence obtained from VT NMR, underlining the role of TEP in promoting Mg^{2+} -OTf $^-$ dissociation and simultaneously diversifying the population fractions with reduced CIP concentration (Figures S32 and S33). DFT results from our previous work⁹ reported a highly exergonic bond dissociation energy (BDE) of -1.25 eV for the C–S bond in a partially reduced Mg^+ -TFSI $^-$ CIP, which became increasingly exergonic in the presence of explicit solvent molecules (Figure S34). The visualized spin density in the dissociated fragments revealed that the thermodynamically favorable electrolyte decomposition enabled the

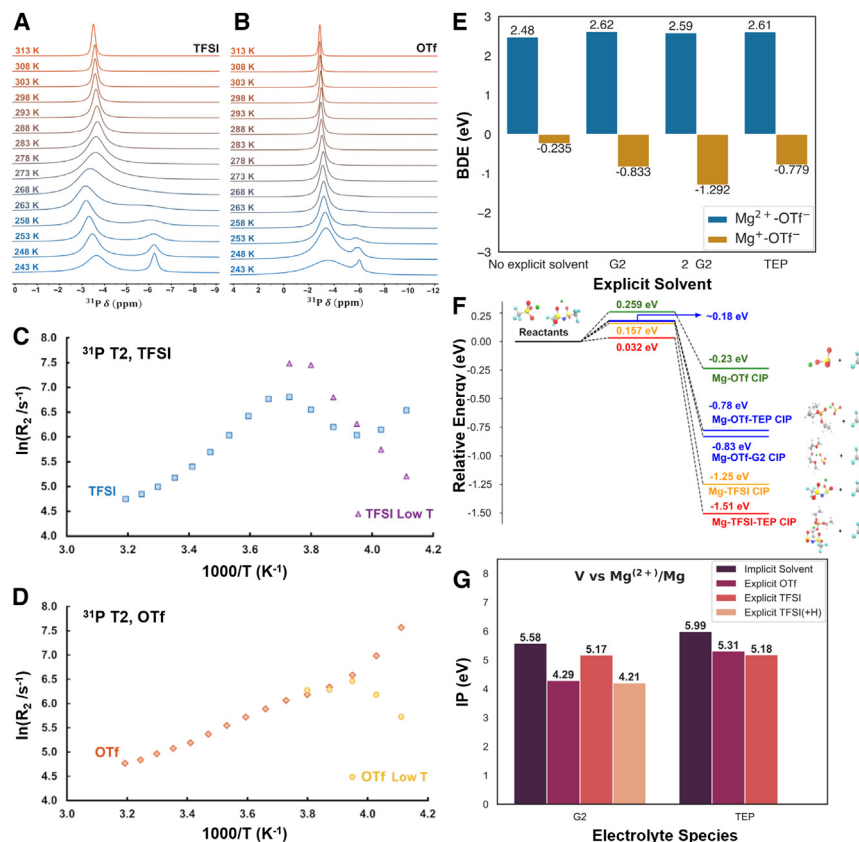


Figure 4. Electrolyte solvation dynamics and DFT analysis of electrolyte stability

(A and B) VT ^{31}P NMR line shapes of the (A) 0.2 M $\text{Mg}(\text{TFSI})_2$ and (B) 0.2 M $\text{Mg}(\text{OTf})_2$ in G2:TEP (3:1 in vol) compositions, from 243 to 313 K, illustrating the appearance of distinct signals for TEP-coordinated Mg^{2+} and TEP-coordinated CIP at low temperature.

(C and D) The corresponding difference in solvation dynamics is quantitatively reflected in the VT ^{31}P T₂ curves for the (C) TFSI and (D) OTf compositions. (E) DFT calculations for thermodynamic C–S bond dissociation energies of $[\text{Mg}-\text{OTf}]$ CIPs in the presence of different explicit solvents.

(F) DFT calculations for the kinetic barriers to bond dissociation for different $[\text{Mg}^{2+}-\text{OTf}^-]$ and $[\text{Mg}^{2+}-\text{TFSI}^-]$ CIPs in different solvation environments.

(G) Effect of explicit solvent and deprotonation on the DFT-calculated adiabatic ionization potentials of different solvent molecules.

complete reduction of Mg^+ to Mg^0 . In comparison to TFSI^- , the BDE for a partially reduced Mg^+-OTf^- CIP in implicit solvent is higher by more than 1 eV (Figure 4E). Similarly, the introduction of explicit solvent molecules increased the exergonicity of the dissociation process, but they were consistently greater when compared with that in the TFSI system (Figure S34).⁹ Although thermodynamically favorable, the kinetic barrier for the C–S dissociation in the Mg^+-OTf^- CIP (Figure 4F) was ~ 0.1 eV greater than the partially reduced $\text{Mg}^+-\text{TFSI}^-$ CIP. The kinetic barriers in the presence of explicit solvents (G2 and TEP) were only slightly lower in the Mg^+-OTf^- CIP. However, in $\text{Mg}^+-\text{TFSI}^-$, optimizations with a G2-explicit solvent molecule led to the spontaneous dissociation of either the C–S or the S–N bond. Even in the presence of a TEP-explicit solvent, the calculated barrier was extremely low (0.032 eV). These results indicate that, in addition to the thermodynamic favorability, the dissociation process in the $\text{Mg}^+-\text{TFSI}^-$ CIPs—especially in the presence of explicit solvents—is near barrierless. In contrast, Mg^+-OTf^- CIPs are not only thermodynamically more stable but also protected by higher kinetic barriers, which potentially explains their intrinsic stability against spontaneous decomposition during cycling.

In addition to the reduction behavior of the triflate salt, we also investigated the oxidative stability for the solvent molecules constituting the electrolyte system. The significant deviation between adiabatic and vertical ionization potentials has been previously discussed.⁵⁹ Moreover, previous studies have also reported

the lowering of the oxidation potential in the presence of an explicit anion when compared with the results from a continuum implicit solvent⁶⁰ (e.g., polarizable continuum model [PCM]⁶¹). As observed in Figure 4G, in an implicit solvent, the adiabatic ionization potentials (vs. Mg^{2+}/Mg) are similar for the G2 and the TEP solvent molecules. Nonetheless, the presence of explicit anions significantly reduces the immunoprecipitation (IP) for the G2 molecules. On the other hand, the oxidative stability of the TEP molecules is preserved. A possible explanation of this enhanced stability is the absence of spontaneous proton transfer in the TEP molecules. DFT calculations (Figure S35) reveal that the oxidation of G2 is accompanied by a spontaneous proton transfer to the anion, which has previously been reported to lower the oxidative stability of solvent molecules.⁶² The enhanced oxidative stability of the TEP molecules can be potentially attributed to its coordination geometry (Figure S35). The coordination in $(\text{OTf}^-)\text{-TEP}^+$ is facilitated by the O atom in the P=O motif, which potentially shields the ethyl groups from participating in a spontaneous proton transfer. The overall analysis of MD, DFT, and VT NMR directly correlates with the significant suppression of electrolyte decomposition relevant to reduced CIPs. We also note the steric effect of solvent molecular structures plays a role (Figure S1): G2, with an extra methoxyethoxy group, results in much faster exchange rate between its bound state and free state than frequently used dimethoxyethane, leading to faster Mg^{2+} desolvation while suppressing the easy decomposition of bound molecules. Furthermore, TEP, with an extra methylene group, greatly increases its stability against reduction during magnesium plating (Figure S36).

Application to a high-areal-capacity full battery with free-standing thin magnesium anode

The reversibility of this magnesium anode and oxidative stability of the electrolyte was further demonstrated in a full cell.

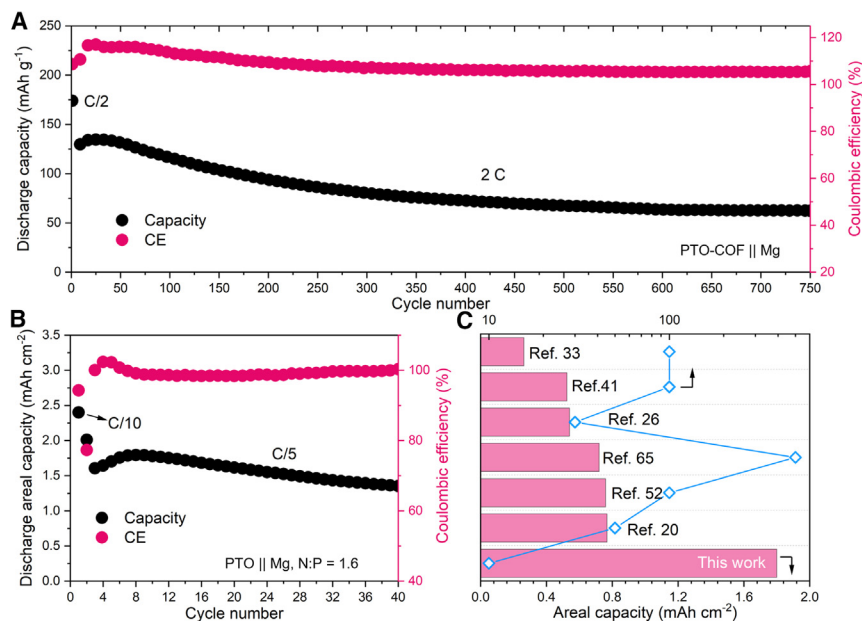


Figure 5. The electrochemistry of full battery with n-type organic cathode materials

(A) The cycling stability of PTO-COF||Mg cell. (B) The cycling stability of high areal capacity PTO||Mg cell where the magnesium was an electrodeposited thin foil with an areal capacity of 4 mAh cm⁻². The CE was calculated as charge capacity divided by discharge capacity because both cells start with discharge. (C) Comparison of areal capacity and the thickness of magnesium anode in this work to that reported elsewhere at room temperature.

Linear sweep voltammetry (LSV) reveals over 4 V anodic stability on various substrates (Figure S37); much higher than conventional chloride-based electrolytes (~2.5 V). Although sulfide-based^{3,63} or conversion-type materials (for example, CuS) (Figure S38),^{64,65} are commonly used as benchmark Mg cathodes, they are limited to low voltages. Therefore, we synthesized an organic n-type pyrene-4,5,9,10-tetraone-based covalent organic framework (PTO-COF, Figure S39) that was previously reported as a high-voltage and high-capacity organic cathode for lithium-ion batteries.⁶⁶ As shown in Figures 5A and S39, PTO-COF shows an initial capacity of ~180 mAh g⁻¹ at C/2 (1 C = 200 mA g_{PTO-COF}⁻¹), with an average voltage of 2.1 V, and can cycle for 750 cycles at a fast rate of 2 C. We ascribe the gradual decrease in capacity and slightly >100% CE to the continuous dissolution of unreacted PTO monomers in this organic cathode material, which has been well-noted in the literature.²⁰ We further used the state-of-art PTO²⁰ as a prototype high-areal-capacity Mg cathode owing to its higher theoretical capacity of 408 mAh g⁻¹. A high-loading PTO cathode (2.5 mAh cm⁻²) was coupled with the electrodeposited, free-standing, 10- μ m-thick magnesium foil at a low negative/positive (N/P) ratio of 1.6. The cell was cycled at C/5 (1C = 408 mA g_{PTO}⁻¹) after one-cycle activation (Figure 5B and S40), exhibiting an areal capacity of 1.8 mAh cm⁻² for over 40 cycles without short circuiting. To our knowledge, this is the first demonstration of magnesium full cells at such high areal capacity with a thin magnesium anode at room temperature (Figure 5C). We also note that the cell-level energy density of such organic RMBs is limited by the carbon content in the cathode (~50 wt %: note <5% discharge capacity contribution; Figure S41).⁶⁷ This could be overcome with improved, dense cathode materials that function at high voltage and take advantage of the desolvation afforded by this electrolyte, albeit being beyond the scope of the present work.

trochemical cycling—which disappears on rest and is restored by pulsing the current.

Such unique interfacial phenomenon is closely related to the kinetic difference of various electro/chemical reactions at the Mg/electrolyte interface. The side reactions between electrolyte and fresh magnesium have very slow kinetics, as verified by DFT. During the dynamic plating process, anions move away from the Mg surface and the Mg deposition kinetics are far faster than electrolyte decomposition: thus, virtually no decomposition occurs that could form an interphase. During the rest, because the Mg electrodeposition is terminated, the exposed fresh Mg deposit can gradually react with electrolyte to form some interphase, as shown via XPS and TOF-SIMS analysis. However, once the fresh Mg deposit is covered by a thin interphase, the electrolyte decomposition will stop due to the contact loss with fresh Mg. Therefore, only a very thin layer of such interphase forms on the Mg surface that has minor impact on Mg diffusion. Once we restore the electrochemical plating/stripping, the clean interface is restored due to the faster kinetics of Mg plating than electrolyte decomposition. The TEM analysis also provides solid evidence that the bulk region of the deposited Mg is clean and free of any electrolyte-derived species. Overall, such a clean interface is stabilized under dynamic plating/stripping due to the kinetic difference between Mg electrodeposition and electrolyte decomposition.

Our approach contrasts that of engineering the electrolyte via additives, which are consumable and form an SEI that hinders Mg²⁺ interfacial diffusion. This strategy thus successfully achieves electrodeposition of densely aligned thin hexagonal magnesium platelets under practical conditions. This leads to a close-to-unity CE of magnesium electrodeposition/stripping at demanding conditions over long-term cycling in both half and full cells. Our understanding, built on the ternary relationship of electrolyte-interphase-morphology, is distinct from conventional concepts of the invaluable role of functional SEIs in ensuring reversible operation of various batteries.

Building on the above insights, the remarkable properties of our electrolyte deliver the possibility to ensure a new generation of high-energy-density RMBs that are comparable or superior to other systems. First, the near-unity CE of magnesium E/S allows the implementation of ultrathin magnesium anodes and hence assembly of cells with low negative:positive (N/P) ratios to benefit energy density. Second, the high boiling points of the solvents (G2:162°C, TEP: 215°C) are much higher than that of commonly used DME (85°C), which is essential for achieving lean electrolyte conditions.²⁶ Third, the high anodic stability of this electrolyte provides excellent compatibility with high-voltage cathodes. Last, the propensity for facile desolvation of Mg^{2+} at the anode that we demonstrate here with $\text{Mg}(\text{OTf})_2/\text{G2}:\text{TEP}$ should also extend to the cathode. This opens up a new avenue for the discovery of possible high-rate and high-voltage/capacity materials—with good electronic conductivity—that may resolve the long-standing question of whether Mg^{2+} -ion diffusion in the bulk or Mg^{2+} -ion desolvation at the interface are the limiting factors at the positive electrode. We expect these insights and design principles can be extended to other multivalent battery systems and stimulate wider research attention.

EXPERIMENTAL PROCEDURES

Preparation of electrolytes

$\text{Mg}(\text{OTf})_2$ (Solvionic, 99.5%) and $\text{Mg}(\text{TFSI})_2$ (Solvionic, 99.5%) were dried in a Buchi vacuum oven at 150°C for over 3 days. DME (Sigma-Aldrich, 99.5%), G2 (Sigma-Aldrich, 99.5%), and TEP (Sigma-Aldrich, $\geq 99.8\%$), were dried over molecular sieves (Sigma-Aldrich, 3 Å) for > 24 h twice before use. All salts, solvents, and additives were stored in an Ar-filled glove box with H_2O and O_2 levels less than 0.1 ppm. To prepare the electrolyte, a weighed mass of $\text{Mg}(\text{OTf})_2$ was added into G2:TEP mixtures at specific volume ratios and the mixture was stirred at 25°C for at least 24 h to fully dissolve the salt.

Electrochemical measurements

Coin cells (2032) with a standard spring were used to investigate the magnesium plating/stripping behavior in both symmetric and asymmetric cells using a VMP3 potentiostat/galvanostat station (Bio-Logic). Magnesium foils (100 μm , Changsha Rich Nonferrous Metals) were polished by sandpaper before being punched into small disks (diameter: 12.7 mm; mass: ~ 18.9 mg) for symmetric cell assembly, and two glass fiber separators (0.7 μm pore size, 475 μm , Sigma-Aldrich) were used (diameter: 16 mm) with 100 μL electrolyte in each cell. The Cu foil (9 μm , MTI Corporation) was washed with ethanol and punched into disks (diameter: 10 mm). Electrochemically polished magnesium electrodes were obtained by cycling a symmetric cell for 5 cycles and then used to assemble asymmetric cells for CE measurements with bare Cu as the working electrode. LSV was performed to measure the anodic stability of the electrolyte at a sweep rate of 1 mV s^{-1} , with magnesium as both the reference and counter electrodes and various metal foils (Pt, Ti, SS, and Al, diameter: 11 mm) as working electrodes. Electrochemical impedance spectroscopy (EIS) was performed on a magnesium symmetric coin cell, with a voltage amplitude of 10 mV in the frequency range of 1 MHz to 100 mHz.

The CuS/C was prepared with a CuS mass ratio of 30%, using our reported method where the presence of porous nitrogen-doped carbon matrix enhances the kinetics of CuS.⁶⁸ The electrode was fabricated by mixing CuS/C (Sigma-Aldrich, 99.99%) and polyvinylidene fluoride at a weight ratio of 9:1 with 1-methyl-2-pyrrolidinone as the dispersion agent. The mixed slurry was coated on copper foil by doctor blading with an active mass loading of ~ 1 mg cm^{-2} . PTO-COF electrode was synthesized following a previous report with a mass loading of ~ 1 mg cm^{-2} .⁶⁶ Polished magnesium foil was directly used as the counter electrode to assemble CuS||Mg and PTO-COF||Mg full cells. For high-loading PTO electrodes, PTO powder (Chemsene) was first ball milled with Ketjen black carbon at a weight ratio of 4:5 for 100 min at

250 rpm. The PTO electrode was fabricated by mixing the above mixture with polytetrafluoroethylene (Sigma-Aldrich, 60 wt % dispersion in H_2O) at a weight ratio of 9:1, using isopropanol as the dispersion agent. The free-standing PTO cathode obtained was dried at 60°C overnight and punched into small disks (diameter: 8 mm) for full-cell assembly. The mass loading for active material is 6.2 mg cm^{-2} . An electrodeposited 10- μm -thick magnesium foil was used as the counter electrode, which is not commercially available because producing such thin foils via mechanical processing is challenging as pure magnesium is brittle and fragile. Following the previous study,²⁶ a graphene oxide (GO) membrane was used to mitigate the shuttling of dissolved Mg_2PTO . Single-layer GO powder (8 mg; H Method, ACS Material) was dispersed in 20 ml ethanol by ultrasonic agitation for 30 min. The free-standing GO membrane was then obtained by a vacuum-filter method, with a mass loading of ~ 0.5 mg cm^{-2} . All cathodes examined in this work were discharged first and the CE was thus calculated by the charge capacity divided by discharge capacity.

Materials characterization

The thin-film magnesium used for characterization was prepared by electrodeposition on a Cu substrate at 2 mA cm^{-2} current density to an areal capacity of 4 mAh cm^{-2} . The Cu electrode with deposited magnesium was disassembled from the cell and washed with DME three times in a vial, after which the thin-film magnesium self-detached from the Cu substrate. After drying in vacuum at 25°C, the thin-film magnesium was transferred into an Ar-filled glovebox for further characterization. Powder X-ray diffraction (XRD) studies were carried out on an X-ray diffractometer using Cu-K α radiation (PANalytical Empyrean) equipped with a PIXcel bidimensional detector. The scanning electron microscopy (SEM) images of Mg plating/stripping morphologies and energy-dispersive X-ray spectra (EDX) were collected on a Zeiss Ultra field emission SEM instrument. XPS experiments were conducted on a Thermo Scientific K-Alpha XPS instrument. CasaXPS software was used to conduct XPS data analysis, where the C 1s peak of 284.8 eV was used to calibrate the binding energies. Spectral fitting was based on Gaussian-Lorentzian functions and a Shirley-type background. The Ar⁺ etching rate was estimated to be ~ 1.0 nm min^{-1} . The ionic conductivity of the electrolyte was measured via an Orion Star A325 pH/Conductivity Meter (Thermo) at 25°C. The detailed procedures of molecular dynamic (MD) simulations and DFT calculations are outlined in supplemental information.

TEM analysis

A cross-sectional lamella for TEM examination was prepared via focused ion beam (FIB) lift-out using a Scios 2 dual-beam FIB/SEM. The region from which the lift-out was taken is indicated by the yellow box in Figure S7A. This area was selected due to its possessing surface fissures but without the topography being too variable in height such that it might risk the structural integrity of the lamella. Figure S7B shows a tilted view of the area after trenching but prior to lift-out and final thinning. The Mg anode was transferred from the argon-atmosphere glove box into the FIB inside an Ar-filled sealed bag to minimize exposure. After the lift-out was completed, the mount holding the grid was transferred back into the glove box using the Ar-filled bag method.

The TEM grid containing the lift-out was loaded into a Gatan 648 air-free transfer holder while inside the Ar-filled glove box. This prevented the sample from exposure to air/moisture during transport and loading into the TEM. At some point between removal of the grid from the FIB and loading into the air-free transfer holder, a portion of the protective Pt cap fell off the lamella. This did not appear to have any meaningful impact on the underlying sample.

Bright-field (BF), dark-field (DF), and high-resolution (HR) conventional TEM images and selected area electron diffraction (SAED) were acquired using an FEI/Thermo Fisher Titan G2 ETEM at an operating voltage of 300 kV and beam dosage of 72 $\text{e}/\text{Å}^2\text{s}$. High-angle annular DF scanning TEM (HAADF-STEM) was performed on a FEI/Thermo Fisher Titan G2 ChemiSTEM equipped with a SuperX EDS detector, at an operating voltage of 200 kV and a probe current of 120 pA. No alteration/damage of the sample during TEM characterization was observed.

TOF-SIMS

TOF-SIMS spectra were collected by an ION-TOF TOF-SIMS 5 machine in negative-ion mode with a 30-keV cluster primary ion gun over an area of 100 \times

100 μm^2 . 256 \times 256 pixels were used to raster this area. The principal ion current was approximately 0.3 pA. The stop condition was set to $5 \times 1,012$ ions per cm^2 for semiquantitative analysis. The 2D images essentially collapse the 3D datasets in one direction parallel to the surface, yielding 2D XZ and YZ images. This method was used to alleviate the variance of homogeneity of different morphologies. The pixel-by-pixel signal intensities in the other surface parallel direction (but perpendicular to X or Y) are summed to create the pixels in the resulting image. The vertical direction in the image shows the surface at the top of the image and the bottom of the profile at the base. The horizontal axis of the image is the lateral dimension of the sputter crater (100 μm).

NMR spectroscopy

All NMR experiments were performed on an 11.7-T magnet with a Bruker Neo console, using a specially modified, broadband-tuning Bruker SmartProbe (with low- γ tuning capability). Both ^{19}F (470.60 MHz Larmor frequency) and ^{31}P (202.47 MHz) were studied, with the former referenced to 0.1 M sodium trifluoroacetate (NaTFA) (aqueous) (at -77 ppm) and the latter to 85% H_3PO_4 (at 0 ppm). ^{25}Mg measurements were also carried out, but the much-reduced sensitivity rendered these impractical for the scope of the current study. Nutation curves collected on the references were used for pulse calibrations, yielding $\pi/2$ pulses of 12.7 μs for ^{19}F and 19.2 μs for ^{31}P . VT experiments were performed with both nuclei for samples of $\text{Mg}(\text{TFSI})_2$ in G2/TEP, $\text{Mg}(\text{OTf})_2$ in G2/TEP, and neat G2/TEP (^{31}P only) over a temperature range of 243–313 K, corrected by the VT unit, which was self-tuned at 298 K. Referencing was performed with the substitution method before and after the VT collection run, with the chemical shifts corrected for magnet drift. Additional NMR methods details are presented in the [supplemental information](#).

RESOURCE AVAILABILITY

Lead contact

Further information and requests for resources and materials should be directed to and will be fulfilled by the lead contact, Linda F. Nazar (lfnazar@uwaterloo.ca).

Materials availability

This study did not generate new unique materials.

Data and code availability

The datasets generated in this study are available from the [lead contact](#) on reasonable request.

ACKNOWLEDGMENTS

This work was financially supported by the Joint Centre for Energy Storage Research, an Energy Innovation Hub funded by the U.S. Department of Energy, Office of Science, Basic Energy Sciences. L.F.N. also acknowledges NSERC for platform support through the Discovery Grant and Canada Research Chair programs. R.D.G. and K.A.P. gratefully acknowledge support from the Battery Materials Research (BMR) program under the Assistant Secretary for Energy Efficiency and Renewable Energy, Office of Vehicle Technologies of the U.S. Department of Energy, contract DEAC02-05CH11231. This research used resources of the National Energy Research Scientific Computing Center (NERSC). This work was performed, in part, at the Center for Integrated Nanotechnologies, an Office of Science User Facility operated for the U.S. Department of Energy (DOE) Office of Science. Sandia National Laboratories is a multimission laboratory managed and operated by National Technology & Engineering Solutions of Sandia, LLC, a wholly owned subsidiary of Honeywell International, Inc., for the U.S. DOE's National Nuclear Security Administration under contract DE-NA-0003525. The views expressed in the article do not necessarily represent the views of the U.S. DOE or the United States Government.

AUTHOR CONTRIBUTIONS

C.L. and L.F.N. designed this study. C.L. prepared the electrolytes and carried out the physical characterization and all the electrochemical measurements.

R.D.G. and K.A.P. performed molecular dynamics and DFT calculations. S.D.H. and K.Z. carried out the S/TEM experiments. J.D.B. performed the NMR measurements. Y.Y. synthesized the CuS/C material. C.L. and L.F.N. wrote the manuscript with contributions from the other authors.

DECLARATION OF INTERESTS

The authors declare no competing interests.

SUPPLEMENTAL INFORMATION

Supplemental information can be found online at <https://doi.org/10.1016/j.joule.2024.11.007>.

Received: August 13, 2024

Revised: October 20, 2024

Accepted: November 11, 2024

Published: December 6, 2024

REFERENCES

1. Mohtadi, R., Tutusaus, O., Arthur, T.S., Zhao-Karger, Z., and Fichtner, M. (2021). The metamorphosis of rechargeable magnesium batteries. *Joule* 5, 581–617. <https://doi.org/10.1016/j.joule.2020.12.021>.
2. Yoo, H.D., Shterenberg, I., Gofer, Y., Gershinsky, G., Pour, N., and Aurbach, D. (2013). Mg rechargeable batteries: an on-going challenge. *Energy Environ. Sci.* 6, 2265–2279. <https://doi.org/10.1039/C3EE40871J>.
3. Aurbach, D., Lu, Z., Schechter, A., Gofer, Y., Gizbar, H., Turgeman, R., Cohen, Y., Moshkovich, M., and Levi, E. (2000). Prototype systems for rechargeable magnesium batteries. *Nature* 407, 724–727. <https://doi.org/10.1038/35037553>.
4. Zhang, H., Qiao, L., and Armand, M. (2022). Organic Electrolyte Design for Rechargeable Batteries: From Lithium to Magnesium. *Angew. Chem. Int. Ed. Engl.* 61, e202214054. <https://doi.org/10.1002/anie.202214054>.
5. Li, M., Lu, J., Ji, X., Li, Y., Shao, Y., Chen, Z., Zhong, C., and Amine, K. (2020). Design strategies for nonaqueous multivalent-ion and monovalent-ion battery anodes. *Nat. Rev. Mater.* 5, 276–294. <https://doi.org/10.1038/s41578-019-0166-4>.
6. Attias, R., Salama, M., Hirsch, B., Goffer, Y., and Aurbach, D. (2019). Anode-Electrolyte Interfaces in Secondary Magnesium Batteries. *Joule* 3, 27–52. <https://doi.org/10.1016/j.joule.2018.10.028>.
7. Sun, Y., Wang, Y., Jiang, L., Dong, D., Wang, W., Fan, J., and Lu, Y.C. (2023). Non-nucleophilic electrolyte with non-fluorinated hybrid solvents for long-life magnesium metal batteries. *Energy Environ. Sci.* 16, 265–274. <https://doi.org/10.1039/D2EE03235J>.
8. Huang, X., Tan, S., Chen, J., Que, J., Que, Z., Deng, R., Long, J., Xiong, F., Huang, G., Zhou, X., et al. (2024). Asymmetric SO_3CF_3 -Grafted Boron-Center Anion Enables Boron-Containing Interphase for High-Performance Rechargeable Mg Batteries. *Adv. Funct. Mater.* 34, 2314146. <https://doi.org/10.1002/adfm.202314146>.
9. Li, C., Guha, R.D., Shyamsunder, A., Persson, K.A., and Nazar, L.F. (2024). A weakly ion pairing electrolyte designed for high voltage magnesium batteries. *Energy Environ. Sci.* 17, 190–201. <https://doi.org/10.1039/D3EE02861E>.
10. Eaves-Rathert, J., Moyer, K., Zohair, M., and Pint, C.L. (2020). Kinetic-versus Diffusion-Driven Three-Dimensional Growth in Magnesium Metal Battery Anodes. *Joule* 4, 1324–1336. <https://doi.org/10.1016/j.joule.2020.05.007>.
11. Zhao, W., Pan, Z., Zhang, Y., Liu, Y., Dou, H., Shi, Y., Zuo, Z., Zhang, B., Chen, J., Zhao, X., et al. (2022). Tailoring Coordination in Conventional Ether-based Electrolytes for Reversible Magnesium-Metal Anodes. *Angew. Chem. Int. Ed. Engl.* 61, e202205187. <https://doi.org/10.1002/anie.202205187>.

12. Du, Y., Chen, Y., Tan, S., Chen, J., Huang, X., Cui, L., Long, J., Wang, Z., Yao, X., Shang, B., et al. (2023). Strong solvent coordination effect inducing gradient solid-electrolyte-interphase formation for highly efficient Mg plating/stripping. *Energy Storage Mater.* 62, 102939. <https://doi.org/10.1016/j.ensm.2023.102939>.
13. Zhang, D., Wang, Y., Yang, Y., Zhang, Y., Zhao, Y., Pan, M., Sun, Y., Chen, S., Liu, X., Wang, J., et al. (2023). Constructing Efficient Mg(CF₃SO₃)₂ Electrolyte via Tailoring Solvation and Interface Chemistry for High-Performance Rechargeable Magnesium Batteries. *Adv. Energy Mater.* 13, 2301795. <https://doi.org/10.1002/aenm.202301795>.
14. Wang, S., Wang, K., Zhang, Y., Jie, Y., Li, X., Pan, Y., Gao, X., Nian, Q., Cao, R., Li, Q., et al. (2023). High-entropy Electrolyte Enables High Reversibility and Long Lifespan for Magnesium Metal Anodes. *Angew. Chem. Int. Ed. Engl.* 62, e202304411. <https://doi.org/10.1002/anie.202304411>.
15. Li, Z., Nguyen, D., Bazak, J.D., Han, K.S., Chen, Y., Prabhakaran, V., Le, T.T., Cheng, Z., Song, M., Pol, V.G., et al. (2024). Stable Cycling of Mg Metal Anodes by Regulating the Reactivity of Mg²⁺ Solvation Species. *Adv. Energy Mater.* 14, 2301544. <https://doi.org/10.1002/aenm.202301544>.
16. Bae, J., Park, H., Guo, X., Zhang, X., Warner, J.H., and Yu, G. (2021). High-performance magnesium metal batteries via switching the passivation film into a solid electrolyte interphase. *Energy Environ. Sci.* 14, 4391–4399. <https://doi.org/10.1039/D1EE00614B>.
17. Son, S.B., Gao, T., Harvey, S.P., Steirer, K.X., Stokes, A., Norman, A., Wang, C., Cresce, A., Xu, K., and Ban, C. (2018). An artificial interphase enables reversible magnesium chemistry in carbonate electrolytes. *Nat. Chem.* 10, 532–539. <https://doi.org/10.1038/s41557-018-0019-6>.
18. Mohtadi, R., Matsui, M., Arthur, T.S., and Hwang, S.J. (2012). Magnesium borohydride: from hydrogen storage to magnesium battery. *Angew. Chem. Int. Ed. Engl.* 51, 9780–9783. <https://doi.org/10.1002/anie.201204913>.
19. Tutusaus, O., Mohtadi, R., Arthur, T.S., Mizuno, F., Nelson, E.G., and Sevryugina, Y.V. (2015). An Efficient Halogen-Free Electrolyte for Use in Rechargeable Magnesium Batteries. *Angew. Chem. Int. Ed. Engl.* 54, 7900–7904. <https://doi.org/10.1002/anie.201412202>.
20. Dong, H., Tutusaus, O., Liang, Y., Zhang, Y., Lebens-Higgins, Z., Yang, W., Mohtadi, R., and Yao, Y. (2020). High-power Mg batteries enabled by heterogeneous enolization redox chemistry and weakly coordinating electrolytes. *Nat. Energy* 5, 1043–1050. <https://doi.org/10.1038/s41560-020-00734-0>.
21. Zhao-Karger, Z., Gil Bardaji, M.E., Fuhr, O., and Fichtner, M. (2017). A new class of non-corrosive, highly efficient electrolytes for rechargeable magnesium batteries. *J. Mater. Chem. A* 5, 10815–10820. <https://doi.org/10.1039/C7TA02237A>.
22. Luo, J., Bi, Y., Zhang, L., Zhang, X., and Liu, T.L. (2019). A Stable, Non-Corrosive Perfluorinated Pinacolatoborate Mg Electrolyte for Rechargeable Mg Batteries. *Angew. Chem. Int. Ed. Engl.* 58, 6967–6971. <https://doi.org/10.1002/anie.201902009>.
23. Herb, J.T., Nist-Lund, C.A., and Arnold, C.B. (2016). A Fluorinated Alkoxyaluminate Electrolyte for Magnesium-Ion Batteries. *ACS Energy Lett.* 1, 1227–1232. <https://doi.org/10.1021/acseenergylett.6b00356>.
24. Pavčnik, T., Lozinšek, M., Pirnat, K., Vizintin, A., Mandai, T., Aurbach, D., Dominko, R., and Bitenc, J. (2022). On the Practical Applications of the Magnesium Fluorinated Alkoxyaluminate Electrolyte in Mg Battery Cells. *ACS Appl. Mater. Interfaces* 14, 26766–26774. <https://doi.org/10.1021/acsaami.2c05141>.
25. Mandai, T., Youn, Y., and Tateyama, Y. (2021). Remarkable electrochemical and ion-transport characteristics of magnesium-fluorinated alkoxyaluminate-diglyme electrolytes for magnesium batteries. *Mater. Adv.* 2, 6283–6296. <https://doi.org/10.1039/D1MA00448D>.
26. Li, S., Zhang, J., Zhang, S., Liu, Q., Cheng, H., Fan, L., Zhang, W., Wang, X., Wu, Q., and Lu, Y. (2024). Cation replacement method enables high-performance electrolytes for multivalent metal batteries. *Nat. Energy* 9, 285–297.
27. Liang, Y., Dong, H., Aurbach, D., and Yao, Y. (2020). Current status and future directions of multivalent metal-ion batteries. *Nat. Energy* 5, 646–656. <https://doi.org/10.1038/s41560-020-0655-0>.
28. Jäckle, M., Helmbrecht, K., Smits, M., Stottmeister, D., and Groß, A. (2018). Self-diffusion barriers: possible descriptors for dendrite growth in batteries? *Energy Environ. Sci.* 11, 3400–3407. <https://doi.org/10.1039/C8EE01448E>.
29. Jäckle, M., and Groß, A. (2014). Microscopic properties of lithium, sodium, and magnesium battery anode materials related to possible dendrite growth. *J. Chem. Phys.* 141, 174710. <https://doi.org/10.1063/1.4901055>.
30. Ling, C., Banerjee, D., and Matsui, M. (2012). Study of the electrochemical deposition of Mg in the atomic level: Why it prefers the non-dendritic morphology. *Electrochim. Acta* 76, 270–274. <https://doi.org/10.1016/j.electacta.2012.05.001>.
31. Li, C., Shyamsunder, A., Key, B., Yu, Z., and Nazar, L.F. (2023). Stabilizing magnesium plating by a low-cost inorganic surface membrane for high voltage and high-power Mg batteries. *Joule* 7, 2798–2813. <https://doi.org/10.1016/j.joule.2023.10.012>.
32. Singh, N., Arthur, T.S., Tutusaus, O., Li, J., Kisslinger, K., Xin, H.L., Stach, E.A., Fan, X., and Mohtadi, R. (2018). Achieving High Cycling Rates via In Situ Generation of Active Nanocomposite Metal Anodes. *ACS Appl. Energy Mater.* 1, 4651–4661. <https://doi.org/10.1021/acsaem.8b00794>.
33. Hou, S., Ji, X., Gaskell, K., Wang, P.F., Wang, L., Xu, J., Sun, R., Borodin, O., and Wang, C. (2021). Solvation sheath reorganization enables divalent metal batteries with fast interfacial charge transfer kinetics. *Science* 374, 172–178. <https://doi.org/10.1126/science.abg3954>.
34. Yang, G., Li, Y., Wang, J., Lum, Y., Lim, C.Y.J., Ng, M.F., Zhang, C., Chang, Z., Zhang, Z., Handoko, A.D., et al. (2024). Realizing horizontal magnesium platelet deposition and suppressed surface passivation for high-performance magnesium metal batteries. *Energy Environ. Sci.* 17, 1141–1152. <https://doi.org/10.1039/D3EE02317F>.
35. Wang, G., Liu, X., Shi, H., Ma, Y., Wang, Z., Sun, C., Song, F., Zhang, Z., Dong, S., Du Sun, M., et al. (2024). Achieving Planar Electroplating/Stripping Behavior of Magnesium Metal Anode for a Practical Magnesium Battery. *ACS Energy Lett.* 9, 48–55. <https://doi.org/10.1002/adma.202401576>.
36. Zheng, J., Zhao, Q., Tang, T., Yin, J., Quilty, C.D., Renderos, G.D., Liu, X., Deng, Y., Wang, L., Bock, D.C., et al. (2019). Reversible Epitaxial Electrodeposition of Metals in Battery Anodes. *Science* 366, 645–648. <https://doi.org/10.1126/science.aax6873>.
37. Zhang, W., Zhao, Q., Hou, Y., Shen, Z., Fan, L., Zhou, S., Lu, Y., and Archer, L.A. (2021). Dynamic Interphase-mediated Assembly for Deep Cycling Metal Batteries. *Sci. Adv.* 7, eabl3752. <https://doi.org/10.1126/sciadv.abl3752>.
38. Zhang, Z., Li, Y., Xu, R., Zhou, W., Li, Y., Oyakhire, S.T., Wu, Y., Xu, J., Wang, H., Yu, Z., et al. (2022). Capturing the swelling of solid-electrolyte interphase in lithium metal batteries. *Science* 375, 66–70. <https://doi.org/10.1126/science.abi8703>.
39. Forero-Saboya, J.D., Tchitcheкова, D.S., Johansson, P., Palacín, M.R., and Ponrouch, A. (2022). Interfaces and Interphases in Ca and Mg Batteries. *Adv. Mater. Interfaces* 9, 2101578. <https://doi.org/10.1002/admi.202101578>.
40. Mandai, T., Tanaka, U., and Watanabe, M. (2024). Mg–Zn–Cl-integrated functional interface for enhancing the cycle life of Mg electrodes. *Energy Storage Mater.* 67, 103302. <https://doi.org/10.1016/j.ensm.2024.103302>.
41. Nguyen, D.T., Eng, A.Y.S., Ng, M.F., Kumar, V., Sofer, Z., Handoko, A.D., Subramanian, G.S., and Seh, Z.W. (2020). A High-Performance Magnesium Triflate-based Electrolyte for Rechargeable Magnesium Batteries. *Cell Rep. Phys. Sci.* 1, 100265. <https://doi.org/10.1016/j.xcrp.2020.100265>.
42. Li, G., Chen, K., Lei, M., Wang, T., Hu, M., and Li, C. (2024). Construction of Fluoride-Rich Interphase for Sustained Magnesiophilic Site Release

- Toward High-Stability Chloride-Free Magnesium Metal Batteries. *Adv. Energy Mater.* **14**, 2401507. <https://doi.org/10.1002/aenm.202401507>.
43. Hu, M., Li, G., Chen, K., Zhou, X., and Li, C. (2024). A gradient structured SEI enabling record-high areal capacity anode for high-rate Mg metal batteries. *Chem. Eng. J.* **480**, 148193. <https://doi.org/10.1016/j.cej.2023.148193>.
44. Zhou, X., Li, G., Yu, Y., Lei, M., Chen, K., and Li, C. (2024). Building Organic-Inorganic Robust Interphases from Deep Eutectic Solution for Highly Stable Mg Metal Anode in Conventional Electrolyte. *Small Methods* **8**, e2301109. <https://doi.org/10.1002/smt.202301109>.
45. Rajput, N.N., Qu, X., Sa, N., Burrell, A.K., and Persson, K.A. (2015). The Coupling between Stability and Ion Pair Formation in Magnesium Electrolytes from First-Principles Quantum Mechanics and Classical Molecular Dynamics. *J. Am. Chem. Soc.* **137**, 3411–3420. <https://doi.org/10.1021/jacs.5b01004>.
46. Liu, X., Du, A., Guo, Z., Wang, C., Zhou, X., Zhao, J., Sun, F., Dong, S., and Cui, G. (2022). Uneven Stripping Behavior, an Unheeded Killer of Mg Anodes. *Adv. Mater.* **34**, e2201886. <https://doi.org/10.1002/adma.202201886>.
47. Song, Z., Zhang, Z., Du, A., Dong, S., Li, G., and Cui, G. (2020). Insights into interfacial speciation and deposition morphology evolution at Mg-electrolyte interfaces under practical conditions. *J. Energy Chem.* **48**, 299–307. <https://doi.org/10.1016/j.jechem.2020.02.019>.
48. Wang, D., Gao, X., Chen, Y., Jin, L., Kuss, C., and Bruce, P.G. (2018). Plating and stripping calcium in an organic electrolyte. *Nat. Mater.* **17**, 16–20. <https://doi.org/10.1038/nmat5036>.
49. Li, C., Jin, S., Archer, L.A., and Nazar, L.F. (2022). Toward practical aqueous zinc-ion batteries for electrochemical energy storage. *Joule* **6**, 1733–1738. <https://doi.org/10.1016/j.joule.2022.06.002>.
50. Matsui, M. (2011). Study on electrochemically deposited Mg metal. *J. Power Sources* **196**, 7048–7055. <https://doi.org/10.1016/j.jpowsour.2010.11.141>.
51. Tang, K., Du, A., Dong, S., Cui, Z., Liu, X., Lu, C., Zhao, J., Zhou, X., and Cui, G. (2020). A Stable Solid Electrolyte Interphase for Magnesium Metal Anode Evolved from a Bulky Anion Lithium Salt. *Adv. Mater.* **32**, e1904987. <https://doi.org/10.1002/adma.201904987>.
52. Blázquez, J.A., Maça, R.R., Leonet, O., Azaceta, E., Mukherjee, A., Zhao-Karger, Z., Li, Z., Kovalevsky, A., Fernández-Barquín, A., Mainar, A.R., et al. (2023). A practical perspective on the potential of rechargeable Mg batteries. *Energy Environ. Sci.* **16**, 1964–1981. <https://doi.org/10.1039/D2EE04121A>.
53. Wen, T., Deng, Y., Qu, B., Huang, G., Song, J., Xu, C., Du, A., Xie, Q., Wang, J., Cui, G., et al. (2023). Re-envisioning the Key Factors of Magnesium Metal Anodes for Rechargeable Magnesium Batteries. *ACS Energy Lett.* **8**, 4848–4861. <https://doi.org/10.1021/acscenergylett.3c01959>.
54. Zhang, J., Liu, J., Wang, M., Zhang, Z., Zhou, Z., Chen, X., Du, A., Dong, S., Li, Z., Li, G., et al. (2023). The origin of anode–electrolyte interfacial passivation in rechargeable Mg–metal batteries. *Energy Environ. Sci.* **16**, 1111–1124. <https://doi.org/10.1039/D2EE03270H>.
55. Yang, Z., Yang, M., Hahn, N.T., Connell, J., Bloom, I., Liao, C., Ingram, B.J., and Trahey, L. (2022). Toward practical issues: Identification and mitigation of the impurity effect in glyme solvents on the reversibility of Mg plating/stripping in Mg batteries. *Front. Chem.* **10**, 966332. <https://doi.org/10.3389/fchem.2022.966332>.
56. Li, Q., Chen, A., Wang, D., Pei, Z., and Zhi, C. (2022). “Soft shorts” hidden in zinc metal anode research. *Joule* **6**, 273–279. <https://doi.org/10.1016/j.joule.2021.12.009>.
57. Adams, B.D., Zheng, J., Ren, X., Xu, W., and Zhang, J.-G. (2018). Accurate Determination of Coulombic Efficiency for Lithium Metal Anodes and Lithium Metal Batteries. *Adv. Energy Mater.* **8**, 1702097. <https://doi.org/10.1002/aenm.201702097>.
58. Bain, A.D. (2003). Chemical exchange in NMR. *Prog. Nucl. Magn. Reson. Spectrosc.* **43**, 63–103. <https://doi.org/10.1016/j.pnmrs.2003.08.001>.
59. Borodin, O., Olguin, M., Spear, C.E., Leiter, K.W., and Knap, J. (2015). Towards high throughput screening of electrochemical stability of battery electrolytes. *Nanotechnology* **26**, 354003. <https://doi.org/10.1088/0957-4484/26/35/354003>.
60. Borodin, O., Ren, X., Vatamanu, J., von Wald Cresce, A., Knap, J., and Xu, K. (2017). Modeling Insight into Battery Electrolyte Electrochemical Stability and Interfacial Structure. *Acc. Chem. Res.* **50**, 2886–2894. <https://doi.org/10.1021/acs.accounts.7b00486>.
61. Tomasi, J., Mennucci, B., and Cammi, R. (2005). Quantum Mechanical Continuum Solvation Models. *Chem. Rev.* **105**, 2999–3093. <https://doi.org/10.1021/cr9904009>.
62. Borodin, O., Behl, W., and Jow, T.R. (2013). Oxidative Stability and Initial Decomposition Reactions of Carbonate, Sulfone, and Alkyl Phosphate-Based Electrolyte. *J. Phys. Chem. C* **117**, 8661–8682. <https://doi.org/10.1021/jp400527c>.
63. Sun, X., Bonnick, P., Duffort, V., Liu, M., Rong, Z., Persson, K.A., Ceder, G., and Nazar, L.F. (2016). A high capacity thiospinel cathode for Mg batteries. *Energy Environ. Sci.* **9**, 2273–2277. <https://doi.org/10.1039/C6EE00724D>.
64. Zhao-Karger, Z., Liu, R., Dai, W., Li, Z., Diemant, T., Vinayan, B.P., Bonatto Minella, C.B., Yu, X., Manthiram, A., Behm, R.J., et al. (2018). Toward Highly Reversible Magnesium–Sulfur Batteries with Efficient and Practical Mg[B(hfip)4]2 Electrolyte. *ACS Energy Lett.* **3**, 2005–2013. <https://doi.org/10.1021/acscenergylett.8b01061>.
65. Chen, Z., Yang, Q., Wang, D., Chen, A., Li, X., Huang, Z., Liang, G., Wang, Y., and Zhi, C. (2022). Tellurium: A High-Performance Cathode for Magnesium Ion Batteries Based on a Conversion Mechanism. *ACS Nano* **16**, 5349–5357. <https://doi.org/10.1021/acsnano.1c07939>.
66. Gao, H., Neale, A.R., Zhu, Q., Bahri, M., Wang, X., Yang, H., Xu, Y., Clowes, R., Browning, N.D., Little, M.A., et al. (2022). A Pyrene-4,5,9,10-Tetraone-Based Covalent Organic Framework Delivers High Specific Capacity as a Li-Ion Positive Electrode. *J. Am. Chem. Soc.* **144**, 9434–9442. <https://doi.org/10.1021/jacs.2c02196>.
67. Bitenc, J., Pirnat, K., Lužanin, O., and Dominko, R. (2024). Organic Cathodes, a Path toward Future Sustainable Batteries: Mirage or Realistic Future? *Chem. Mater.* **36**, 1025–1040. <https://doi.org/10.1021/acs.chemmater.3c02408>.
68. Yu, Y., Singh, B., Yu, Z., Kwok, C.Y., Kochetkov, I., and Nazar, L.F. (2024). A Nanocrystallite CuS/Nitrogen-Doped Carbon Host Improves Redox Kinetics in All-Solid-State Li 2 S Batteries. *Adv. Energy Mater.* **14**, 2400845. <https://doi.org/10.1002/aenm.202400845>.